



Direct Numerical Simulation of Aero-Optical Effects in Hypersonic Flow Over a Three-Dimensional Bump

Max C. Walker¹, Neil D. Sandham²

1. Abstract

Direct numerical simulations (DNS) of a three-dimensional bump on a flat plate are carried out to analyse stability and aero-optic effects in a hypersonic flow field. Bumps are a canonical configuration for shock-wave boundary-layer interactions (SWBLI), which generate a system of shock waves and expansion fans due to geometrical influence. Adverse pressure gradients cause boundary layer separation on both sides of the bump, sustaining instabilities and potentially leading to transition. In compressible flow, aero-optical effects arise from light traversing density fluctuations, where different parts of a wavefront experience varying refractive indices, resulting in image distortion at the aperture. Optical windows require thermal protection due to extreme heating, and cooling methods such as film injection and suction vents are commonly employed. This study compares several blowing and suction configurations, evaluating their impact on both heat flux and optical distortion. The Mach 4 inflow condition corresponds to Mach 6 flight at 28 km altitude, and the DNS captures fine-scale turbulence and shock interactions. The optical path difference (OPD) calculations are validated against the Notre Dame semi-empirical model, showing agreement in attached boundary layers. Results demonstrate that suction schemes reduce downstream heat flux by up to 20% and improve optical performance, while blowing introduces mixing-layer turbulence that can degrade image quality. The study provides insight into the trade-offs between thermal protection and optical clarity, offering guidance for flow control strategies in hypersonic sensor design.

Keywords: Aero-optics, bumps, flow control, SWBLI

Nomenclature

(x, y, z) = spatial coordinates u, v, w = velocity components

 ρ = density

p = pressure

T = temperature

 $\mu = viscosity$

 M_{∞} = Mach number

Re =Reynolds number

Pr = Prandtl number

 γ = specific heat ratio

a =speed of sound

 U_{∞}^* = freestream velocity [m/s]

 $\mu_{\infty}^* = \text{freestream viscosity } [kg/(m s)]$

 T_{∞}^* = freestream temperature [K]

 p_{∞}^* = freestream pressure $[kg/m s^2]$

SWBLI = Shock-Wave/Boundary-Layer

Interaction

DNS = Direct Numerical Simulation

LES = Large Eddy Simulation

WMLES = Wall-modelled Large Eddy

Simulation

OPL = Optical Path Length

OPD = Optical Path Difference

HiSST-2025-0107
Direct Numerical Simulation of Aero-Optical Effects of Hypersonic Flow Over a Bump

Copyright

¹ Postgraduate researcher, Aerodynamics and Flight Mechanics Group, University of Southampton, SO17 1BJ, United Kingdon, E-mail: m.c.walker@soton.ac.uk

² Professor of Aerospace Engineering, *Aerodynamics and Flight Mechanics Group, University of Southampton, SO17 1BJ, United Kingdon,* E-mail: n.sandham@soton.ac.uk

2. Introduction

At hypersonic conditions, geometrical protrusions from a surface, such as those associated with optical sensing, experience extreme heat fluxes and aerodynamic instabilities. Shock-waves caused by deflected streamlines create higher flow temperatures as the gas is abruptly slowed across the discontinuity. These shocks lead to a separation of the boundary layer which can be highly three-dimensional and act as a catalyst for further instabilities downstream. The resulting instabilities can have an adverse effect on the optical performance of sensors on a hypersonic vehicle.

The study of optical effects through boundary layers began in the 50's with experimental studies [1], but with recent advances in computational resource for high fidelity flow simulations there is more interest in using numerical methods for predicting aero-optical effects. These have historically been time averaged, magnitude predictions using statistical models, which do not allow for understanding of adaptive-optical corrections [2]. Time accurate and computationally expensive simulations are required to understand the relationship between continuous wavefront phase change and the unsteady turbulent flow.

Optical distortions occur from density perturbations as light moves through a medium, which becomes significant in highly compressible flows. As the light travels through the changing density field, adjacent beams of the wavefront traverse at different speeds leading to distortion. Distortions that arise from density perturbations are often described by the Optical Path Difference (OPD) along the path of the light ray from the object that a sensor is capturing. Many investigations into aero-optical effects have focused on distortions through subsonic turbulent boundary layers. However, at supersonic speeds, shock-turbulence interactions pose further computational challenges [3] as discontinuities and compressibility effects play a larger role.

Hypersonic vehicles rely on sensors to navigate and track targets. These sensors sit behind windows that experience high temperatures due to convective heat transfer. Due to the critical conditions of the materials, active cooling methods are required to reduce the heat fluxes to the vehicle surface, with injection of cooled gas being a popular choice. A balance must be made for the injection of gas to sufficiently cool the surface whilst ensuring that the optical measurements are not degraded. Torres et al. [4] looked at cooling films of varying gases over an optical window for a Mach 2 flow, to investigate the aero-optical effects through the mixing layer. They found that the cooling film produced a highly turbulent mixing layer at the boundary between the outer boundary layer and the cooled gas, where the coherent structures produced significant optical distortions.

Arunajatesan and Sinha [5] used time accurate large eddy simulation (LES) results of supersonic flow past a turret finding that the shock-wave in front of the turret, along with the separation bubble upstream, led to very strong degradation of a beam pointing upstream. The degradation was much less for beams pointing downstream and to the side. Turrets are a closer resemblance to the present study, whereas most OPD results have been shown for flat plates or backwards facing steps. Zou et al. [6] and Li et al. [7] both looked at supersonic to hypersonic flow, over a flat plate and an infrared seeker head respectively. They employed blowing and suction schemes upstream of the optical windows to determine whether flow control methods can reduce aero-optical effects. Both papers point to a significant improvement in the temperature profiles downstream with greater flow uniformity. Zou et al. reported that suction schemes maintained a laminar boundary layer downstream, improving the Optical distortions by 70%-80% with constant suction amplitudes of 0.1-0.2 of freestream velocity. They found that cool air injection can improve the thermal performance downstream but may introduce unwanted disturbances having a less useful impact on the optical performance. Li et al. similarly found suction to be much more effective than blowing, with blowing showing a negative impact on the optical results. They found a 14.7% improvement at Mach 3 and 20% at Mach 5 for the suction cases.

Castillo et al. [8] used a wall modelled large eddy simulation (WMLES) code to simulate Mach 8 flow over a flat plate with an isothermal wall and compared against Sandia National Laboratories conditions. These results are plotted onto the Notre-Dame empirical model [9]. They found extremely good agreement for their Mach 2 results, with only a 4.5% deviation. At higher Mach numbers, compressibility and non-equilibrium effects that are not considered in this model become more pronounced and it was

noted that a refined model may be required when venturing into higher Mach number cases with larger temperature gradients.

This study will look to further the understanding of aero-optical affects in hypersonic flows over threedimensional protrusions. Section 3 will outline the numerical methods used and the approach to analyse the optical effects. Section 4 will show the parametric study of blowing and suction schemes, comparing the optical performance of each against the baseline case.

3. Numerical methods

3.1. The governing equations

The compressible Navier-Stokes equations are considered in dimensionless form for this work. Variables are normalised with respect to freestream quantities at the inflow to the computational domain. The velocity components (u, v, w) are normalised with the freestream velocity U_{∞}^* , while the temperature, viscosity, and density are normalised with $T_{\infty}^*, \mu_{\infty}^*, \rho_{\infty}^*$ respectively. Pressure and time are respectively normalised by the dynamic pressure $(\rho_{\infty}^* U_{\infty}^{*2})$ and $\delta_0^* / U_{\infty}^*$ where δ_0^* is the displacement thickness at the domain inlet. The Reynolds number uses the inflow displacement thickness as the reference length, Re = $(\rho_{\infty}^* U_{\infty}^* \delta_0^*) / \mu_{\infty}^*$. The dimensionless Prandtl number (Pr) and the specific heat ratio (γ) are given as 0.72 and 1.4 respectively for a perfect gas model that is applicable in the cold hypersonic flow regime. The conservation of mass, energy and momentum are given below in Einstein notation for three spatial directions x_i (i = 1,2,3)

$$\frac{\partial \rho}{\partial t} + \frac{\partial \rho u_j}{\partial x_i} = 0, \tag{1}$$

$$\frac{\partial \rho u_i}{\partial t} + \frac{\partial \rho u_i u_j}{\partial x_i} = -\frac{\partial P}{\partial x_i} + \frac{\partial \tau_{ij}}{\partial x_i},\tag{2}$$

$$\frac{\partial E}{\partial t} + \frac{\partial (\rho E + P)u_i}{\partial x_i} = -\frac{\partial q_i}{\partial x_i} + \frac{\partial u_i \tau_{ij}}{\partial x_j},\tag{3}$$

with the heat flux tensor and the symmetric viscous stress tensor defined by

$$q_i = \frac{-\mu}{(\gamma - 1)Re \Pr M_{\infty}^2} \frac{\partial T}{\partial x_i},\tag{4}$$

$$\tau_{ij} = \frac{\mu}{Re} \left(\frac{\partial u_j}{\partial x_i} + \frac{\partial u_i}{\partial x_j} - \frac{2}{3} \frac{\partial u_k}{\partial x_k} \delta_{ij} \right), \tag{5}$$

with Sutherland temperature being $T_s^* = 110.4 \text{ K}$. The speed of sound and pressure for a chosen Mach number M_{∞} , are given as

$$a = \sqrt{\frac{\gamma p}{\rho}} \text{ and } p = \frac{1}{\gamma M_{\infty}^2} \rho T.$$
 (6)

3.2. Numerical scheme and case setup

The simulation of turbulence in a supersonic flow with strong shock waves requires a method that can capture small scale turbulent structures while maintaining stability in the vicinity of discontinuities. In the present study, a fifth order Weighted Essentially Non-Oscillatory (WENO) shock capturing scheme [10] is used for the Euler terms, while the viscous and heat conduction terms are handled with a fourth-order central differencing scheme extended to the wall [11]. A third-order Runge-Kutta scheme was used for time advancement. A no-slip isothermal boundary condition is imposed on the lower wall. The inlet of the domain is set using a similarity solution of the laminar boundary layer equation. A pressure extrapolation condition is applied at the outlet and a zerogradient outlet on the top far-field. The OpenSBLI/OPS code generation system [12] [13] [14] was used to generate CUDA code for running on NVIDIA A100 GPUs and MPI for running on CPUs.

The lower wall geometry is shown in Fig 1 where the peak of the bump is situated 58 units from the inflow. The front face is angled at 30° from horizontal and the bump has a height of 10 inflow displacement thicknesses, δ_0^* , at the peak.

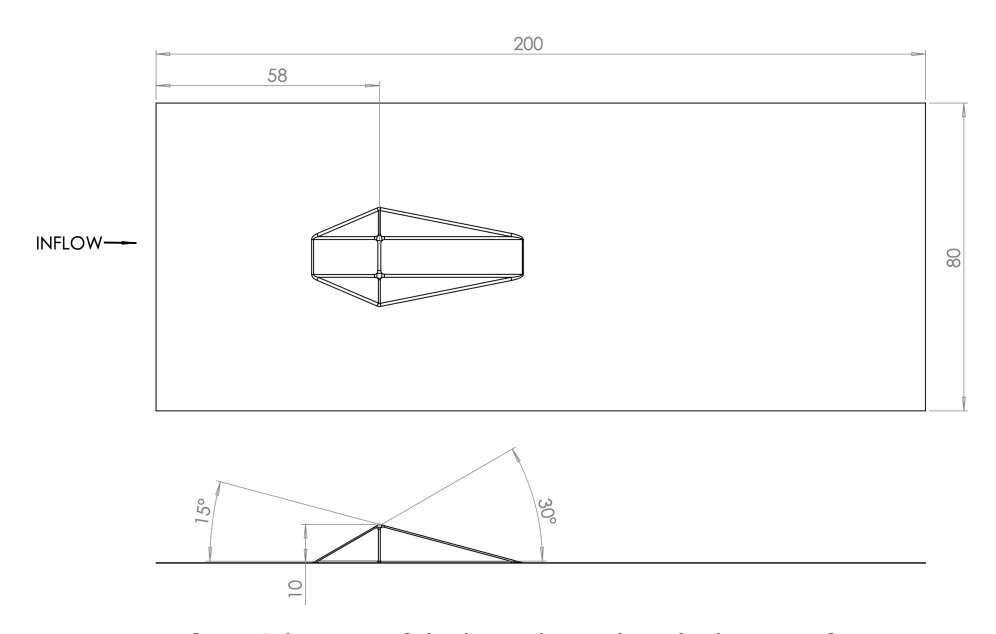


Fig 1. Schematic of the bump located on the lower surface.

Table 1 shows the parameters for this simulation. A grid of 1500x200x800 was chosen based on a grid sensitivity study that was carried out using skin friction, wall pressure and turbulent wall parameters to demonstrate grid independent results. Based on flight conditions of Mach 6 at 28km altitude, a leading edge half wedge angle was chosen as 15° which gives a Mach 4 inflow for this simulation with a post-shock freestream temperature of 439K. A cooled wall of 900K is initialised with a Reynolds number of 4000 based on the inflow displacement thickness, placing the center of the bump 0.227m downstream of the leading edge.

Table 1. Simulation parameters.

| Grid density | θ_b | M_{∞} | $Re_{\delta_0^*}$ | T_{∞} | T_w | γ |
|--------------|------------|--------------|-------------------|--------------|-------|-----|
| 1500x200x800 | 30° | 4.0 | 4000 | 439 K | 900 K | 1.4 |

Fig. 2 shows a density field contour plot of the midspan plane. The view has been zoomed in to the bump for clarity. Aero-optical effects will be analysed from within the bump looking upstream through the boundary layer and shock-wave as shown. For the current study, a viewing angle (θ_t) of 0° will be used, looking directly upstream of the bump, parallel to the wall.

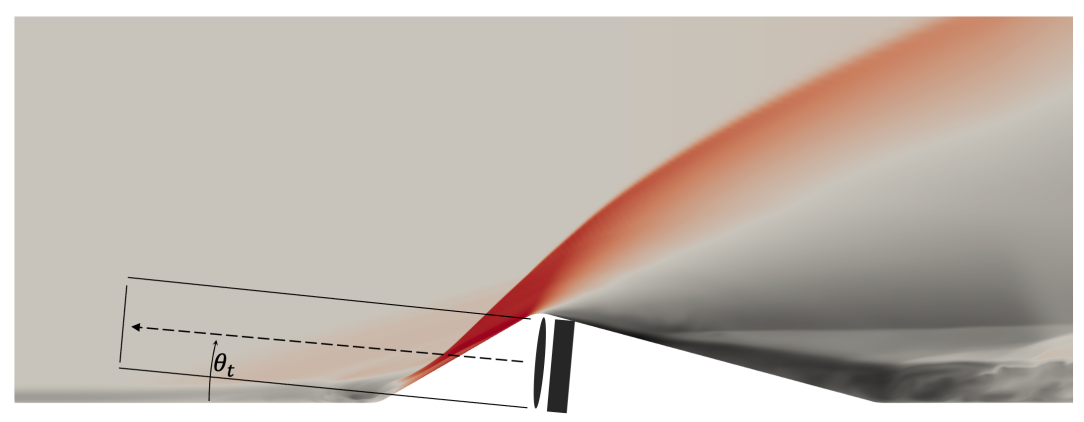


Fig 2. Zoomed midspan instantaneous density field depicts an optical schematic of an optical window looking upstream from the bump.

3.3. Optical path methodology

To determine the extent of distortion for optical performance, the refractive index must be integrated from the aperture along the beam. The fundamental equation that must be solved for a beam propagating through a flow field is the Eikonal equation [5]

$$|\nabla S|^2 = n^2,\tag{7}$$

where S is the wavefront vector $(S(\vec{r}))$ and n is the refractive index, which is a function of density and beam wavelength. By explicitly writing the gradient function, the equation can be expanded and rearranged for integration in the y-direction as

$$\frac{\partial S}{\partial y} = \sqrt{n^2 - \left(\frac{\partial S}{\partial x}\right)^2 - \left(\frac{\partial S}{\partial z}\right)^2}.$$
 (8)

For beams predominantly propagating along the y-axis, the transverse gradients are small and can be neglected. Since the Eikonal, S, represents the accumulated phase, it is redefined as the optical path length. This leaves

$$\frac{\partial OPL}{\partial y} = \sqrt{n^2},\tag{9}$$

which gives the integral

$$OPL(x, z, t, y_{fs}) = \int_0^{y_{fs}} n(x, y, t, y_{fs}) dy$$
 (10)

where the subscript fs stands for freestream. As mentioned, n is a function of density and wavelength, such that

$$n(x, z, t, y_{fs}) = 1 + k_{GD}\rho(x, y, z, t).$$
 (11)

Here, K_{GD} is the Gladstone-Dale constant, which is a function of the beam wavelength and the density is interpolated from the flow field to the beam. By integrating through the density field, the optical path length can be found and used to find the OPD

$$OPD(x, z, t) = OPL(x, z, t) - \overline{OPL(x, z, t)}.$$
 (12)

3.4. Blowing and suction boundary condition

The isothermal boundary condition applied at the lower wall requires adaptation to allow for temperature and velocity to be functions of x and z for these schemes. The original wall temperature, T_{W} , will be applied everywhere other than at the location of injection where the temperature will be the injected temperature, T_{inj} . To simulate a blowing geometry with a more rectangular appearance, a hyperbolic tangential function, shown below, is used where the temperature function in the streamwise direction is given by

$$T = T_W + \frac{(T_{inj} - T_W)(\tanh(x - s_u) - \tanh(x - s_d))}{2},$$
(13)

where s_u and s_d are the upstream and downstream locations of the beginning and end of the blowing zone. This equation is then incorporated into the energy equation at the wall. To simulate the blowing of this cooler gas up the bump, the no slip condition is modified using the same shape as for the temperature. The no-slip condition is replaced by the equation

$$\rho u = \frac{\rho u_{inj}(\tanh(x - s_u) - \tanh(x - s_d))}{2},\tag{14}$$

with ρv handled in the same way. The values of u_{ini} and v_{ini} are arranged to blow at the desired angle to the local surface based on the velocity magnitude required.

Fig. 4 shows a contour plot of the streamwise velocity component, zoomed to make the bump clear. This is the contour of a 30° bump with no blowing, which will be referred to as the base case. Underneath the bump there are four coloured lines with arrows pointing from the surface. These are the four blowing cases that have been run for comparison. The orange case has blowing immediately upstream of the

bump, on the horizontal wall, at an angle of 30° to be parallel with the bump surface. It is being injected at 20% of the freestream velocity for 35 < x < 40 ($s_u = 35$ and $s_d = 40$). The other three cases have blowing for 42 < x < 45 at 1% of the freestream velocity for the green and red cases and 5% for the purple case. The green case has a jet angled at 20° to the local surface and the red and purple are angled at 60° from the surface. All cases have an injected wall temperature of $T_{inj} = 1.2$ which is significantly lower than the fixed wall temperature of $T_W = 2.05$. Table 2 Shows the configurations of each case with their respective labels.



Fig 3. - Diagram to show the cases for cool air injection and where the blowing is applied relative to the bump.

| | - | - | | |
|------|--|-----------------------|-----------|--|
| Case | location | $\boldsymbol{\theta}$ | Amplitude | |
| B1 | 35 <x<40< td=""><td>30°</td><td>20%</td></x<40<> | 30° | 20% | |
| B2 | 42 <x<45< td=""><td>20°</td><td>1%</td></x<45<> | 20° | 1% | |
| B3 | 42 <x<45< td=""><td>60°</td><td>1%</td></x<45<> | 60° | 1% | |
| B4 | 42 <x<45< td=""><td>60°</td><td>5%</td></x<45<> | 60° | 5% | |

Table 2. Case configurations for blowing

The profiles of temperature, streamwise and wall-normal velocity are shown in Fig 4 where varying degrees of blowing and amplitudes are shown based on the amount of u and v required.

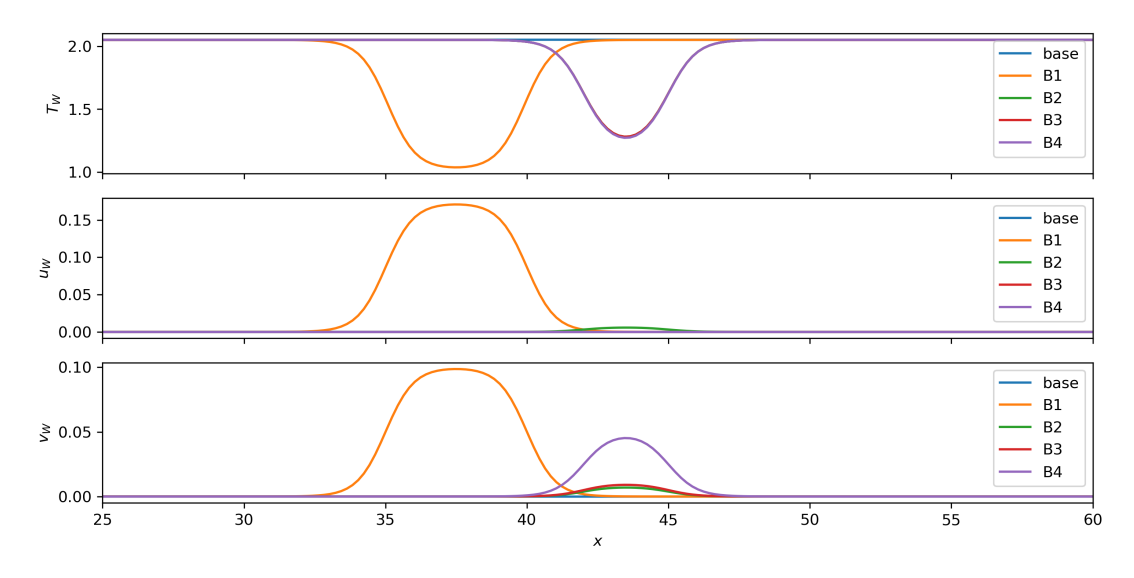


Fig 4. Boundary condition at the wall for temperature, streamwise velocity and wall normal velocity for all four cases.

4. Results

4.1. Validation

The simulation was run for two through flows after the initial transient period and the instantaneous flow field data was analysed. To validate the results obtained for optical distortions through the bump, OPD normalisations have been given by Jumper and Gordeyev [9] for distortions through a turbulent boundary layer at varying Mach numbers. The empirical model developed by the Notre Dame group using experimental results is shown in Fig 6. A section of the density field is chosen to calculate the root mean square of the OPD in the wake region behind the bump as shown in Fig 5, depicting a density field plan view, 20 grid points form the wall (within the boundary layer). This section was chosen as it is not directly downstream of the bump, mitigating any additional distortions due to the separation region and shock wave.

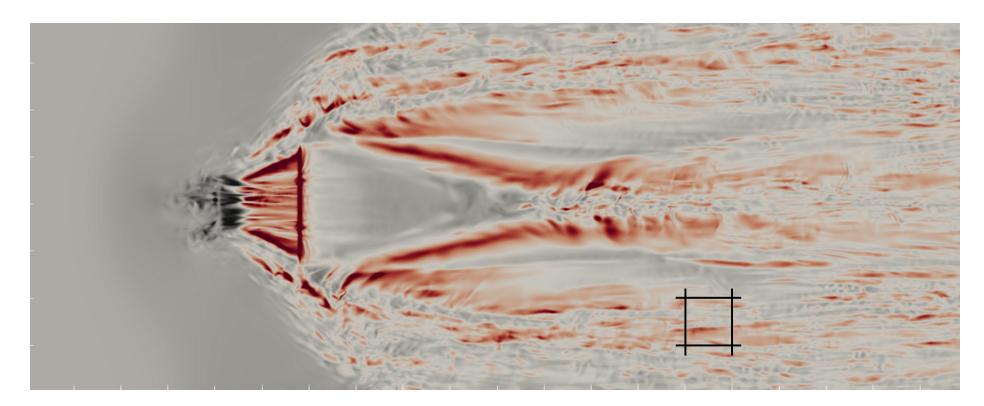


Fig 5. Plan view density field contours close to the wall showing the location for OPD averaging across the turbulent boundary layer region

The normalisation for this model is given by local $K_{GD}\delta\rho_{\infty}M_{\infty}^2\sqrt{C_f}$ where $K_{GD}=2.27x10^{-4}~m^3/kg$ for air and visible wavelengths [15][16], the boundary layer thickness $\delta=6.9\delta_0^*$, freestream density $\rho_{\infty}=0.078~kg/m^3$, Mach number $M_{\infty}=4$ and the averaged skin friction over that region $C_f=0.0235$. After computing the OPD_{rms} within the chosen region, the normalised value is given as 0.0992 which has been plotted on Fig 6 with a red box. This would suggest that the approach to calculating the optical path difference in our simulations is correct, and there can be higher confidence in extending the approach taken to integrating upstream from the bump.

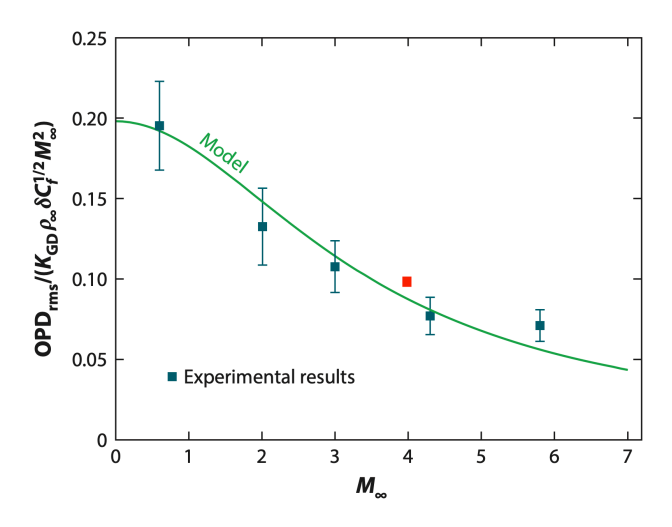


Fig 6. OPD normalisation (figure from Jumper and Gordeyev [9]) with a red box indicating the results from these simulations.

4.2. Blowing cases

The objective of introducing blowing is to reduce the heat flux to the surface. Plotted in Fig 7 is the wall normal gradient of temperature, evaluated from the first grid point off the wall for all 4 cases

which is a surrogate for surface heat flux. The base case has a peak heat flux at around x = 46 and then tapers off towards the peak of the bump at x=58. The second case shows a lower peak heat flux, but with an increase upstream of the bump, possibly showing that the recirculation of the separation bubble is causing the cool air to convect upstream. The heat flux for x > 52 is higher than the base case. For the other three cases, with blowing at 42 < x < 45, the peak heat flux is reduced in all cases from the base value, and the blowing of 1% amplitude leads to an earlier peak. Downstream of the blowing, all cases seem to improve the heat flux slightly, however the only case that seems to sustain an improvement up to around x=55 is the third case (B3). The other two have an adverse effect on the heat flux after $x \approx 52$. From this figure, the third case blowing at 60° at 1% amplitude seems to have the most improvement.

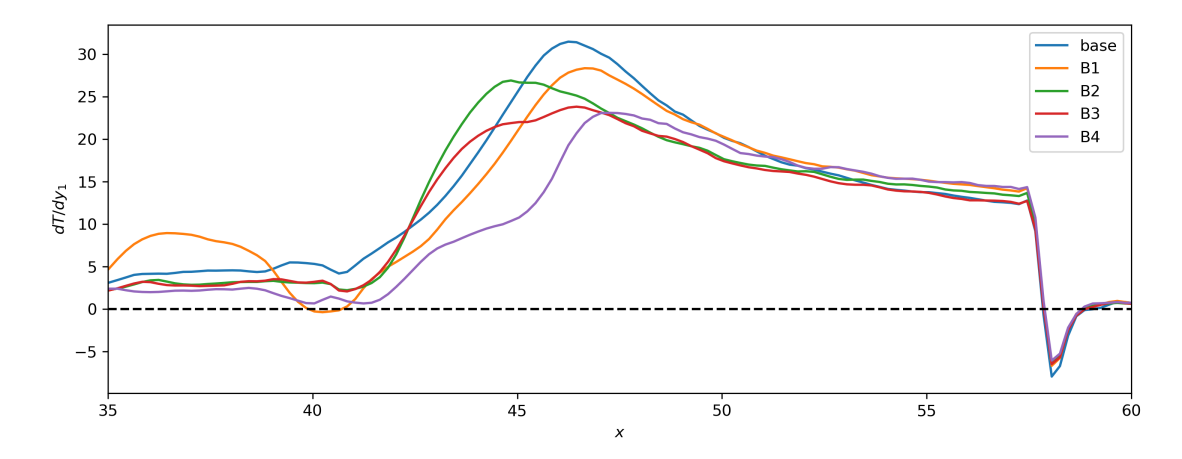


Fig 7. A graph to show the temperature gradient at the wall for blowing cases.

For qualitative comparison, two downstream locations were chosen at x=52 and x=55 where the value of dT/dy_1 for each case was recorded in Table 3. The values are recorded for each location where the difference is shown from the base case and the percentage change from the base value is calculated. The first blowing case, B1, shows an increase in heat flux from the base with almost 10% more heat transfer at x=55. The only case that shows an improvement in the heat flux at both locations is case B3, with 5% improvement at x=52 but only 0.6% at x=55. All other cases showed an increase in the temperature gradient at the wall.

| | anage anange an m | | blowing cases | aan comige | | |
|------|-------------------|---|----------------|--------------------|---|----------------|
| | | | x=55 | | | |
| Case | dT∕dy₁ | Δ | difference (%) | dT/dy ₁ | Δ | difference (%) |
| hase | 16 57 | 0 | 0.0% | 13.74 | 0 | 0.0% |

3.61%

-2.18%

-4.72%

0.25%

15.10

14.41

13.66

14.99

1.36

0.66

-0.08

1.25

0.60

-0.36

-0.78

0.04

Table 3. Percentage change in heat flux from the base for each configuration at two locations for

4.3. Suction cases

B1

B₂

B3

B4

Only one blowing case was found to have an improvement on the temperature gradient at the wall. An alternative approach to reduce the heat flux is to use suction at the slit location rather than blowing. This would simulate a boundary layer bleed system, in which bleed slots or ducts remove the low-momentum, high-temperature boundary layer air from the wall, creating a cooler region downstream. The cases tested were suction at 10 degrees into the surface and suction normal to the surface at the location 42 < x < 45 and another 10° suction at 44 < x < 47. The configuration for suction cases can be found in Table 4.

17.17

16.21

15.79

16.61

9.87%

4.84%

-0.57%

9.09%

Table 4. Case configurations for suction

| Case | location | θ | Amplitude |
|------|---|------|-----------|
| S1 | 42 <x<45< td=""><td>-10°</td><td>10%</td></x<45<> | -10° | 10% |
| S2 | 42 <x<45< td=""><td>-90</td><td>10%</td></x<45<> | -90 | 10% |
| S3 | 44 <x<47< td=""><td>-10°</td><td>10%</td></x<47<> | -10° | 10% |

The temperature gradient at the wall for each case can be seen in Fig 8 with comparison to the base case again. There is a clear improvement of the gradient downstream of the suction for all cases, up to the top of the bump, unlike any blowing case. The peak heat flux is much greater for all cases which is to be expected at the location of suction as hot gas is being drawn into the suction system. The large heat flux at these locations is artificial due to the imposed wall temperature, therefore the focus for the suction cases is on the thermal benefits downstream of the slit.

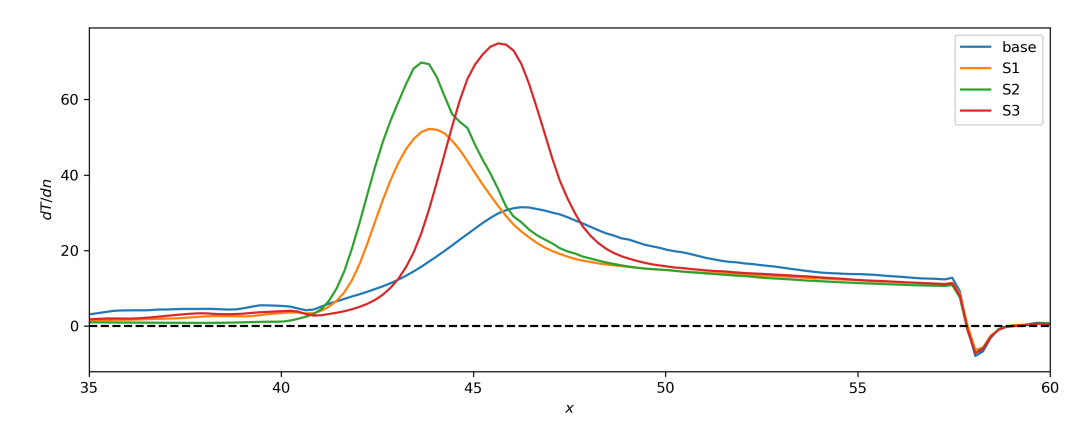


Fig 8. A graph to show the temperature gradient at the wall for suction cases.

Table 5 shows the percentage difference of these cases from the base case at x = 52 and x = 55 for suction. All cases show more than 15% reduction in heat flux at x = 52 and 10% at x = 55 where most blowing cases showed an adverse change in heat flux at the aft location. The configuration with the most noticeable improvement is case S2 where a 20% reduction in heat flux is recorded at the first location. These results show that a suction of hot gas at the wall rather than blowing cooler gas from the surface can have a positive impact on the energy transferred to the surface, in agreement with [6][7].

Contours of temperature can demonstrate whether these mechanisms create cool regions further up the bump and close to the wall. Fig 9 shows the difference in temperature contour for each case from the base temperature field for the blowing cases (9a) and for the suction cases (9b). White regions show areas where the temperature has been unaffected, blue areas have been cooled and red have heated up. The blowing cases seem to show that the boundary layer has heated up downstream, but each sub-figure includes a zoomed inset to look at the near wall region where a dotted line indicates $\Delta T = 0$. This highlights that the first two cases have a region very close to the wall where the temperature is less than the base case. Figure 9b shows a very different impact on the temperature where case S2 has a clear cooler stream closer to the wall than any other sub figure.

Table 5. Percentage change in heat flux from the base for each configuration at two locations for suction cases

| | | x = 52 | | | x = 55 | |
|------|--------------------|--------|----------------|--------------------|--------|----------------|
| Case | dT/dy ₁ | Δ | difference (%) | dT/dy ₁ | Δ | difference (%) |
| Base | 16.57 | 0 | 0.0% | 13.74 | 0 | 0.0% |
| S1° | 13.58 | -2.99 | -18.03% | 12.09 | -1.65 | -11.99% |
| S2° | 13.21 | -3.36 | -20.29% | 11.36 | -2.38 | -17.33% |
| S3° | 14.03 | -2.54 | -15.32% | 12.17 | -1.57 | -11.46% |

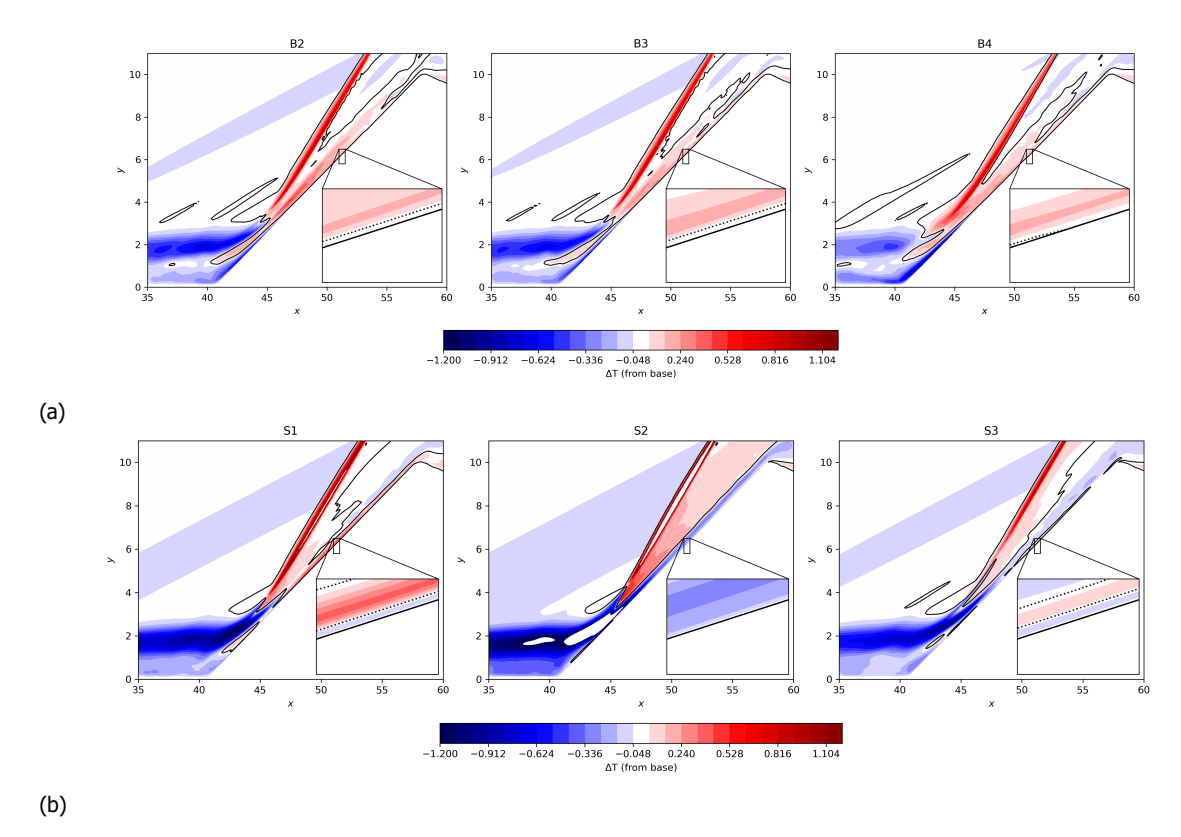


Fig 9. Temperature difference from the base contour plots for the blowing cases (a) and the suction cases (b).

4.4. Aero-optics

Looking directly upstream from the front face of the bump, following a beam path using the integration method of finding the optical path difference from section 3.3, Fig 10 shows a contour representation of the amount of OPD, with red contours showing areas of higher distortions. The central region has the highest values which is consistent with the density field. Fig 2 and Fig 5 show side and top views respectively of the density field at the same moment in time, with a shockwave in front of the bump that seems to be strongest above the lower corner. There are larger distortions looking higher through the flow with OPD increasing at around y=2, in line with the beginning of the shockwave. This agrees with the literature [3] where discontinuities were shown to pose higher risk of optical aberrations and distortions.

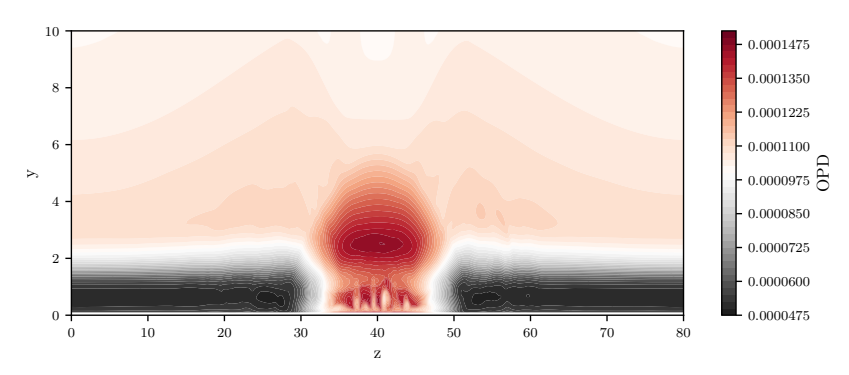


Fig 10. OPD visualisation at x = 10 to show the distortion through the upstream boundary layer

The difference in OPD relative to the base case is shown in Fig 11(a) for the blowing case B3 and for S2 in Fig 11(b). White regions show no change in optical performance whereas red is greater and grey/black is a reduction in optical distortions. The blowing case shows that more distortions are seen in the separation region below the blowing with very little impact in the location of the blowing or

downstream. The performance seems to be unaffected downstream of the blowing, but the reattachment is located within the blowing strip which may cause upstream convection of the injected air to propagate upstream. For the suction case, there is an increase in OPD in the separation region as well, but it seems to have a spanwise effect where optical performance either side of the bump appears to be affected by this implementation, possibly by the introduction of new spanwise vortices. A dotted rectangle has been included to clarify where the suction takes place on the bump. The darked region above it shows a clear improvement in the aero-optical performance above the suction slit. This would suggest that blowing does not have a detrimental effect on the aero-optics whereas suction improved it. Both cases influence the separation region and the suction case increases the distortions around the side of the bump which might affect the sensors field of view in the spanwise direction. Overall, the blowing shows little change in optical performance whereas suction has clear regions of improvement but also regions of higher distortions.

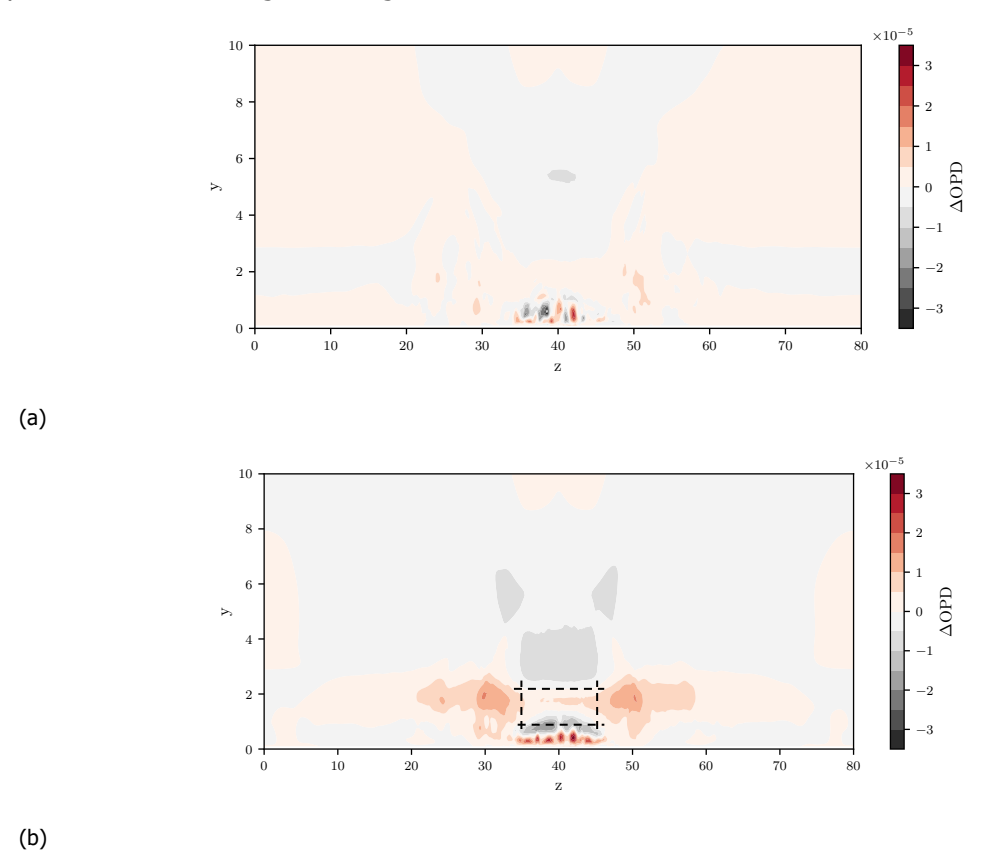


Fig 11. Contours of OPD difference from the base case for case B3 (a) and S2 (b).

5. Conclusions

This study delivers high-fidelity direct numerical simulations of hypersonic flow over a three-dimensional bump, revealing critical insights into aero-optical distortions and thermal mitigation strategies. The simulations confirm that shock-induced separation and reattachment significantly impair optical performance, with the highest OPD values found when looking upstream through a separated flow region. Validation against the Notre Dame empirical model demonstrates strong agreement in attached boundary layers. Suction schemes generally outperformed blowing in both thermal and optical results. Suction reduced downstream heat flux by up to 20% and enhanced optical clarity near the wall by promoting a cooler, more uniform boundary layer. The results suggest that passive or active suction mechanisms, such as boundary layer bleed systems, may offer a more robust solution for protecting optical sensors in hypersonic vehicles. Notably, suction normal to the surface yielded the most significant thermal benefits, while also improving aero-optical performance in the immediate downstream region. However, spanwise distortions introduced by suction highlight the need for careful geometric design to avoid compromising the sensor's field of view.

6. Acknowledgments

The authors acknowledge the use of the IRIDIS High Performance Computing Facility, and associated support services at the University of Southampton, in the completion of this work, as well as the UK Turbulence Consortium under grant EP/X035484/1 for the computational time on the UK national high performance computing facility ARCHER2. MCW is supported by a studentship from UK Missile Defence Centre.

References

- 1. Liepmann, H. W. "Deflection and Diffusion of a Light Ray Passing through a Boundary Layer". Tech. Rep. SM-143997. Santa Monica Division, Santa Monica, Ca: Douglas Aircraft Company, 1952.
- 2. Tyson, Robert K. Principles of Adaptive Optics. San Diego: Academic Press, 1991.
- 3. Wang, Meng, Ali Mani, and Stanislav Gordeyev. "Physics and Computation of Aero-Optics." Annual Review of Fluid Mechanics 44, no. 1 (January 21, 2012): 299–321. https://doi.org/10.1146/annurev-fluid-120710-101152.
- 4. Torres, Roberto, Pedro Castillo, Andreas Gross, Aaron Fassler, Sergey B. Leonov, and Stanislav Gordeyev. "Wall-Modeled Large-Eddy Simulations of Species-Mismatched Supersonic Mixing Layers for Aero-Optical Analysis." In AIAA SCITECH 2025 Forum. Orlando, FL: American Institute of Aeronautics and Astronautics, 2025. https://doi.org/10.2514/6.2025-2767.
- 5. Arunajatesan, Srinivasan, and Neeraj Sinha. "Analysis of Line of Sight Effects in Distortions of Laser Beams Propagating Through A Turbulent Turrent Flow Field." In 43rd AIAA Aerospace Sciences Meeting and Exhibit. Reno, Nevada: American Institute of Aeronautics and Astronautics, 2005. https://doi.org/10.2514/6.2005-1081.
- 6. H. Zou, X.-L. Yang, X.-W. Sun, W. Liu, and Q. Yang. Effective aero-optical suppression by steady wall blowing and wall suction schemes for supersonic turbulent boundary layer. The Aeronautical Journal, 127(1312):1037-1047, June 2023. ISSN 0001-9240, 2059-6464. doi: 10.1017/aer.2022.84. URL https: //www.cambridge.org/core/product/identifier/S0001924022000847/type/iournal article.
- 7. Yubo Li, Shuanghou Deng, Caijun Xue, and Tianhang Xiao. Correction of Aero-Optical Effect with Blow-Suction Control for Hypersonic Vehicles. Applied Sciences, 14(15):6653, July 2024. ISSN 2076-3417. doi: 10.3390/app14156653. URL https://www.mdpi.com/2076-3417/14/15/6653.
- 8. Castillo, Pedro, Andreas Gross, Nathan E. Miller, Kyle P. Lynch, and Daniel R. Guildenbecher. "Numerical Investigation of Wall-Cooling Effect on Aero-Optical Distortions for Hypersonic Boundary Layer." AIAA Journal 61, no. 5 (2023): 1911–24. https://doi.org/10.2514/1.J062570.
- 9. Jumper, Eric J., and Stanislav Gordeyev. "Physics and Measurement of Aero-Optical Effects: Past and Present." Annual Review of Fluid Mechanics 49, no. 1 (January 3, 2017): 419-41. https://doi.org/10.1146/annurev-fluid-010816-060315.
- 10. Shu, Chi-Wang, "Essentially Non-Oscillatory and Weighted Essentially Non-Oscillatory Schemes for Hyperbolic Conservation Laws." In Advanced Numerical Approximation of Nonlinear Hyperbolic Equations: Lectures given at the 2nd Session of the Centro Internazionale Matematico Estivo (C.I.M.E.) Held in Cetraro, Italy, June 23–28, 1997, edited by Bernardo Cockburn, Chi-Wang Shu, Claes Johnson, Eitan Tadmor, and Alfio Quarteroni, 325-432. Lecture Notes in Mathematics. Berlin, Heidelberg: Springer, 1998. https://doi.org/10.1007/BFb0096355.
- 11. Carpenter, Mark H, Jan Nordström, and David Gottlieb. "A Stable and Conservative Interface Treatment of Arbitrary Spatial Accuracy." Journal of Computational Physics 148, no. 2 (1999): 341-65. https://doi.org/10.1006/jcph.1998.6114.

- 12. Lusher, David J., Satya P. Jammy, and Neil D. Sandham. "OpenSBLI: Automated Code-Generation for Heterogeneous Computing Architectures Applied to Compressible Fluid Dynamics on Structured Grids." Computer Physics Communications 267 (2021): 108063. https://doi.org/10.1016/j.cpc.2021.108063.
- 13. Lusher, David J., Andrea Sansica, Neil D. Sandham, Jianping Meng, Bálint Siklósi, and Atsushi Hashimoto. "OpenSBLI v3.0: High-Fidelity Multi-Block Transonic Aerofoil CFD Simulations Using Domain Specific Languages on GPUs." Computer Physics Communications 307 (2025): 109406. https://doi.org/10.1016/j.cpc.2024.109406.
- 14. Reguly, Istvan Z., Gihan R. Mudalige, and Michael B. Giles. "Loop Tiling in Large-Scale Stencil Codes at Run-Time with OPS." IEEE Transactions on Parallel and Distributed Systems 29, no. 4 (April 1, 2018): 873–86. https://doi.org/10.1109/TPDS.2017.2778161.
- 15. Stanislav Gordeyev, Jacob A. Cress, Adam Smith, and Eric J. Jumper. Aero-optical measurements in a subsonic, turbulent boundary layer with non-adiabatic walls. Physics of Fluids, 27(4):045110, April 2015. ISSN 1070-6631, 1089-7666. doi: 10.1063/1.4919331. URL https://pubs.aip.org/pof/article/27/4/045110/1021256/Aero-optical-measurements-in-a-subsonic-turbulent.
- Kan Wang and Meng Wang. Aero-optics of subsonic turbulent boundary layers. Journal of Fluid Mechanics, 696:122–151, April 2012. ISSN 0022-1120, 1469-7645. doi: 10.1017/jfm.2012. URL https://www.cambridge.org/core/product/identifier/S0022112012000110/type/journal_article.

HiSST-2025-0107
Direct Numerical Simulation of Aero-Optical Effects of Hypersonic Flow Over a Bump Copyrig